Journal of the Physical Society of Japan **84**, 094401 (2015)
http://dx.doi.org/10.7566/JPSJ.84.094401

Structural Evolution of a Granular Pack under Manual Tapping

Naoki Iikawa[1], Mahesh M. Bandi[2], and Hiroaki Katsuragi[1*]

[1]*Department of Earth and Environmental Sciences, Nagoya University, Nagoya 464-8601, Japan*
[2]*Collective Interactions Unit, OIST Graduate University, Onna, Okinawa 904-0495, Japan*

(Received March 11, 2015; accepted June 26, 2015; published online August 7, 2015)

We experimentally study a two-dimensional (2D) granular pack of photoelastic disks subject to vertical manual tapping. Using bright- and dark-field images, we employ gradient-based image analysis methods to analyze various structural quantities. These include the packing fraction (ϕ), force per disk (F_d), and force chain segment length (l) as functions of the tapping number (τ). The increase in the packing fraction with the tapping number is found to exponentially approach an asymptotic value. An exponential distribution is observed for the cumulative numbers of both the force per disk $F_d : N_{cum}(F_d) = A_F \exp(-F_d/F_0)$, and the force chain segment length $l : N_{cum}(l) = A_l \exp(-l/l_0)$. Whereas the coefficient A_F varies with τ for F_d, l shows no dependence on τ. The τ dependences of F_d and ϕ allow us to posit a linear relationship between the total force of the granular pack $F^*_{tot}(\tau)$ and $\phi(\tau)$.

1. Introduction

Granular packing is ubiquitous in everyday life. It is common knowledge that a denser granular pack can be achieved by tapping the pack. A clogged granular flow can be unjammed and structural foundations of buildings strengthened by tapping. Indeed, the first thing one does when in trouble with handling granular materials is to tap the container. Nevertheless, the physical mechanisms concerning the effect of tapping on granular packs are not yet completely understood. Recent investigations on granular compaction have used the dimensionless maximum acceleration $\Gamma = \alpha_{max}/g$ to characterize the strength of tapping and/or vibration applied to a granular pack, where α_{max} is the maximum acceleration and $g = 9.8\,\mathrm{m/s^2}$ is the gravitational acceleration.[1–11] Most previous studies have used steady vibration to cause granular compaction. The final state attained by steady vibration is solely determined by Γ.[2,3,6,10,11] The most efficient compaction is induced at a Γ of $\simeq 2$.[2,3,7] When Γ is too small, the compaction takes a long time and grows logarithmically over time. When Γ is too large, on the other hand, it is difficult to attain the highly compacted state as a large amount of kinetic energy is delivered to the granular pack in such a strong vibration.[7] However, granular compaction also depends on the vibration history.[4,5] Although steady vibration has a well-defined maximum acceleration, it represents one particular instance of granular compaction. In general, natural vibration or tapping applied to a granular pack is somewhat irregular. Hence, granular compaction induced by irregular perturbations such as manual tapping must be examined to understand the compaction processes that occur in nature.

To diagnose the physical mechanism of granular compaction, access to the inner stress structure created by a granular pack is necessary. In general, granular packs exhibit an inhomogeneous stress distribution, which can be characterized by a network of force chains. This force chain structure is peculiar to granular assemblies and causes their complex rheological behaviors. The force chain structure can be visualized in a two-dimensional (2D) case. Using a 2D pack of photoelastic disks, the force chains can be observed via the retardation due to the stress-induced birefringence of a photoelastic material.[12–18] Using photoelastic disks, the force applied to each disk can be measured.[12,13] More recently, the applied force has been decomposed into normal and tangential components by a computational image-matching method.[14,16] Relationships among the shearing, isotropic compression, and jamming have been extensively studied using photoelastic disks.[14–18] To the best of our knowledge, however, the tapping-induced granular compaction has not been studied with photoelastic disks. Therefore, we carry out an experiment with photoelastic disks toward clarifying the physics of granular compaction via manual tapping.

In this paper, we report the details of an experimental methodology developed to study granular compaction. A 2D granular pack consisting of photoelastic disks is constructed. Then, manual taps are applied to the granular pack. The evolution of the packing fraction and the force chain structure in the granular pack are characterized by the image analysis of photoelastic disks. On the basis of analysis, the relationship between the packing fraction and the force chain structure is discussed to reveal what happens in the compacted granular pack.

2. Experiment

2.1 Setup

The experimental setup, as shown in Fig. 1, consists of a 2D experimental chamber constructed with acrylic plates along the front and back and held together by aluminium bars along the sides and bottom. The chamber dimensions are $0.3 \times 0.5 \times 0.011\,\mathrm{m^3}$ in height, width, and thickness, respectively. An accelerometer (EMIC 710-C) is mounted on the top-right corner of the chamber to measure the maximum acceleration (α_{max}) experienced during the experiment. The chamber is filled with a bidisperse (to avoid crystallization) set of 350 large (diameter is 0.015 m) and 700 small (diameter is 0.01 m) photoelastic disks of 0.01 m thickness (Vishay Micro Measurements PSM-4). The chamber is vertically placed between a circularly polarized LED light source and a CCD camera (Nikon D70), which acquires two types of image 2000×3008 pixels in size, corresponding to a spatial resolution of 1.76×10^{-4} m/pixel (MPP). The camera is placed 1 m in front of the experimental chamber. First, a bright-field image [Fig. 2(a)] of the granular pack is acquired to measure the packing fraction and the disk centers and diameters for estimation of the force per disk. A second dark-field image [Fig. 2(b)] is acquired by placing a second circular polarizer between the experimental chamber and the

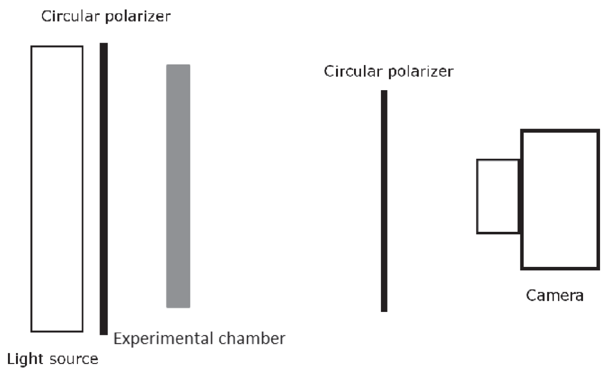

Fig. 1. Top view of the optical setup of the experiment. The experiment is carried out in a dark-room to prevent stray light. The distance between the light source and the camera is about 1 m to ensure uniform angles of incident light into the camera. The 2D experimental chamber is placed vertically in front of the light source, which is attached to a circular polarizer. A snapshot of the chamber is taken with a CCD camera (Nikon D70). The circular polarizer in front of the camera is set at 90° (cross-polarization mode) relative to the other. Two types of images are obtained with and without the circular polarizer in front of the camera.

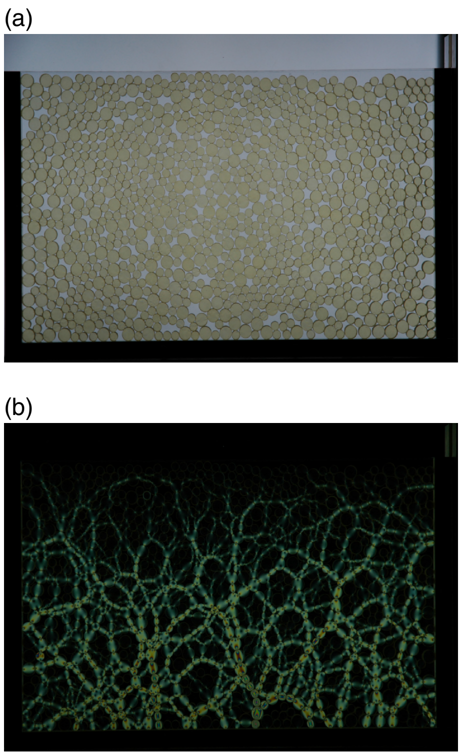

Fig. 2. (Color online) (a) Example of a bright-field image by which the packing fraction and the position of photoelastic disks are obtained. (b) Corresponding dark-field image by which the structure of the force chains is analyzed.

camera in cross-polarization mode. This image provides the photoelastic intensities of the granular force chains. Images are acquired under dark-room conditions to minimize ambient noise from extraneous illumination.

2.2 *Experimental protocol*

Prior to start of the experiment, an initial configuration of low packing fraction is generated. It is preferable that the initial packing fraction be small since this study focuses on granular compaction via manual tapping. However, when disks are introduced in a vertically standing chamber, initial compaction occurs from disk impacts. Therefore, the disks were introduced by spreading them in the chamber while it is horizontally laid down, and then the chamber was vertically fixed, thus assuring a small initial packing fraction. A pair of bright- and dark-field images is then acquired for this initial configuration.

The system is then perturbed by providing a manual tapping to the experimental chamber. In particular, each manual tapping is defined as adding two impulses to each bottom edge of the experimental chamber. Whereas this tapping protocol is not systematically controlled as in the case of an electromagnetic shaker, for instance, it was specifically chosen to mimic the situation of stochastic impulse forcing observed in many natural processes. In any event, the accelerometer attached to the experimental chamber measures the acceleration experienced during tappings, from which dimensionless acceleration is defined as $\Gamma \equiv \alpha_{\max}/g$. The experiments reported here are in the regime of $\Gamma \simeq 3$–4. This tapping acceleration is large enough to achieve the efficient compaction. Following each manual tap, a pair of bright- and dark-field images is acquired for subsequent analysis to determine the evolution in the packing fraction (ϕ), force per disk (F_d), and the force chain segment length (l) as functions of the tapping number (τ). Each experimental run consists of the initial configuration followed by nine manual taps ($\tau = 9$), thus providing ten pairs of bright- and dark-field images per run. Nine experimental runs under identical experimental conditions were conducted.

2.3 *Image analysis*

Here, we explain the image analysis methods employed to extract the packing fraction ϕ, the force per disk F_d, and the force chain segment length l from the bright- and dark-field images. The image analysis software ImageJ[19] was used to analyze the experimental image data.

2.3.1 *Determination of packing fraction*

In this study, we define the packing fraction as $\phi = S_t/(S_m + S_v)$, where S_t is the theoretical total area of the photoelastic disks, S_m is the total area of photoelastic disks measured from the bright-field images, and S_v is the total void area measured from the bright-field images. Whereas theoretically, $S_t = S_m$, in reality, $S_m/S_t \simeq 1.1$ owing to the optical distortion of the image between the center and edges of the bright-field image [see Fig. 2(a)] and the thickness gap between the disks and the chamber wall. When granular compaction occurs under manual tapping, whereas S_m remains almost constant, S_v decreases owing to the reduction in the area of the voids between disks. Therefore, a measurable increase in the packing fraction is observed with increasing tapping number τ. Often, the packing fraction is calculated as the ratio of the area occupied by the photoelastic disks to the total chamber area. This definition is reasonable when the granular pack is enclosed on all sides. However, since this experiment is conducted with the upper side of the experimental chamber left open, an accurate estimation of the total chamber area is not possible. The same situation also arises in the estimation of the packing fraction for granular heaps or sand piles.[20]

For the calculation of the packing fraction ϕ, the theoretical area of the disks S_t was first calculated from the known numbers of large and small disks, whose diameters were already available, yielding $S_t = 1.17 \times 10^{-1}$ m^2 for the experiments reported here. For the calculations of S_m and S_v, the bright-field image was first binarized using ImageJ, which resulted in dark disks on a bright background. The pixel area of the dark regions multiplied by the spatial resolution (MPP) then provided S_m, and the inversion of images was used to obtain S_v.

2.3.2 *Characterization of photoelastic intensity gradient*

Extant studies have used photoelastic signals to measure contact forces in one of two ways. The first method estimates the force per disk using the photoelastic intensity gradient.[12,17] The second method estimates the force per disk via computational image matching.[14,16] In this study, we apply the former method for measurement of the force per disk as the image resolution obtained is insufficient to measure forces by the latter computational matching scheme. The algorithm applied here for force measurement is similar to that adapted by Howell et al.[12]

For the given intensity I for each image pixel (8 bit, gray scale), a Sobel filter was applied to obtain the squared horizontal $(\nabla I_h)^2$ and vertical $(\nabla I_v)^2$ gradients of the intensity. Their sum $|\nabla I|^2 = (\nabla I_h)^2 + (\nabla I_v)^2$ provides the squared gradient of the intensity per pixel. The mean-squared intensity gradient over all pixels within a disk was then defined as $\langle G^2 \rangle \equiv \langle |\nabla I|^2 \rangle$. The computation of $\langle G^2 \rangle$ on each disk requires knowledge of each disk center and its area; information available from the bright-field image (Fig. 3) is obtained in three steps: (1) binarizing a bright-field image, (2) splitting disk areas of contiguous binarized intensity into individual disks, and (3) measuring each disk center position and area. Step 1 is identical to the packing fraction measurement method. In step 2, a watershed algorithm was employed to discriminate between sharp gradients of the intensity among disks, usually referred to as mountains (low-intensity gradient) and rivers (high-intensity gradient), to distinguish individual disks. This is necessary to identify the disk perimeters along which the photoelastic intensities of contact forces exist. Following this watershed procedure, each disk center position and area were measured in step 3. By applying these results to the dark-field image, the mean squared intensity gradient of the photoelastic signal $\langle G^2 \rangle$ was then obtained for each disk.

2.3.3 *Force calibration*

The force per disk was calibrated using a vertical one-dimensional (1D) chain and the measurement method explained in Sect. 2.3.2 to obtain force calibration curves which convert $\langle G^2 \rangle$ to force. A vertical 1D chain of photoelastic disks of 0.3 m height as shown in Figs. 4(a) and 4(b) was constructed. The 1D chain consisted of either 20 large disks or 30 small disks. A pair of bright- and dark-field images was then obtained, and the image analysis methods (Sect. 2.3.2) were applied to calculate $\langle G^2 \rangle$ for each photoelastic disk. $F_c(n)$ in Newtons (where n is the position of the disk from the top of the 1D chain), i.e., the applied force per disk in the vertical 1D chain, was estimated from the relationship $F_c = nmg$, where m is the mass per disk

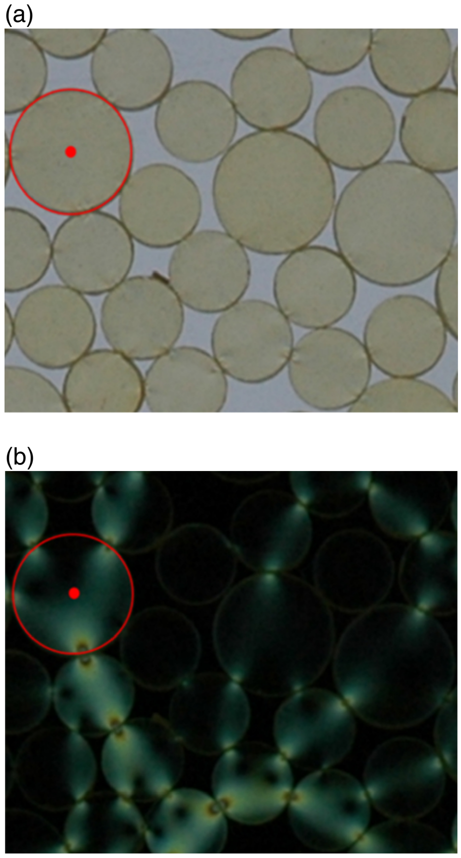

Fig. 3. (Color online) Disk identification and measurement of force per disk from image analysis. The area and center of each disk are obtained from the bright-field image (a). A sample disk center and circumference are shown in red for a large disk. This information is then used in the corresponding dark-field image (b) to obtain the photoelastic signal at disk contacts, and subsequent analysis is employed to measure the force per disk.

(1.8×10^{-3} kg for a large disk and 0.8×10^{-3} kg for a small disk). In Fig. 4(b), fringes on the boundary between disks and sidewalls cannot be observed in the dark-field image. Therefore, the effect of sidewalls was neglected in calibration measurements. Figure 4(c) shows the calibration data obtained for both disk sizes. The quadratic fits of the calibration data were then used as the final calibration curves for measurements of the force per disk in the experimental data. Since the adopted procedure does not involve the computational image matching of photoelastic fringes, only the total force applied to a disk can be measured in this study, which cannot be decomposed into the normal and tangential components.

2.3.4 *Force chain segment length measurement*

The segment length l of force chains forms one of the structural variables measured in this experimental study. We employed a standard image analysis technique known as the thinning method, an example of which is shown in Fig. 5. A dark-field image [Fig. 5(a)] was binarized [Fig. 5(b)] and a skeletonize procedure (also known as the erosion method or the bleeding algorithm) in ImageJ was used to thin the segment down to a line of single-pixel thickness. The force chain segment length was then defined as the linear distance between intersections or end points of the chain in the thinned force chain image [Fig. 5(c)].

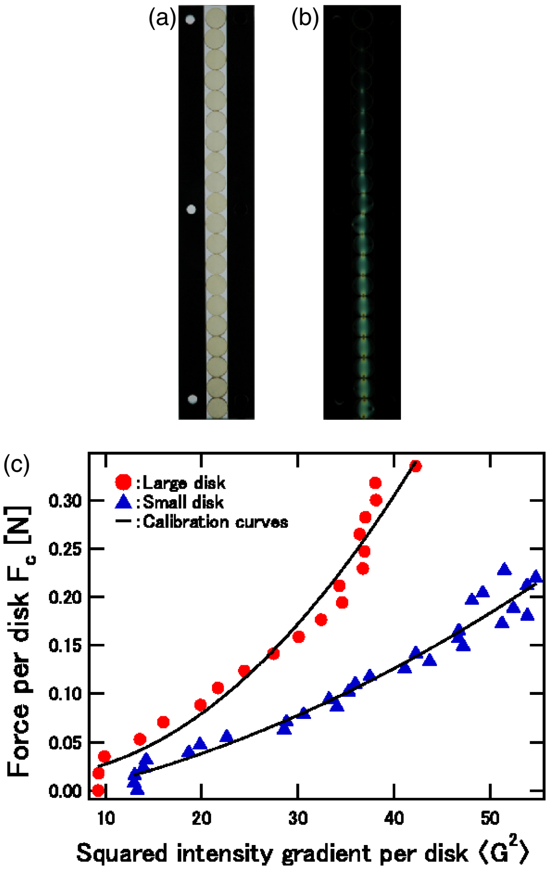

Fig. 4. (Color online) Calibration method using a vertical 1D chain of photoelastic disks. (a) Bright- and (b) dark-field images of the vertical 1D chain. Analysis of the 1D chain images using algorithms explained in Sect. 2.3.2 provided the values of $\langle G^2 \rangle$. (c) The force per disk estimated from the gravitational forcing F_c was then used to relate F_c and $\langle G^2 \rangle$ for both large (solid red circles) and small (solid blue triangles) disks. Solid lines through the calibration data are quadratic fits, which were used in the experimental measurement of the force per disk F_d.

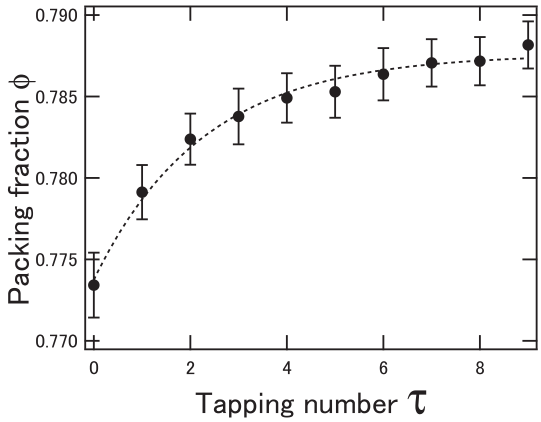

Fig. 6. Variation of packing fraction with manual tapping. The packing fraction increases with each manual tapping and approaches the steady state ($\phi_0 = 0.79$). The mean value of nine runs is shown, and the error bars represent the standard error of nine runs. The dotted curve is the fit, $\phi(\tau) = \phi_0 + A\exp(-\tau/\tau_0)$, where $\phi_0 = 0.79$, $A = -1.39 \times 10^{-2}$, and $\tau_0 = 2.27$ are the values obtained for the fit parameters.

3. Results

3.1 *Packing fraction*

The calculated results for the packing fraction at each tapping number τ are shown in Fig. 6, where $\tau = 0$ represents the initial configuration. The experimental data for $\phi(\tau)$ are fit with the function $\phi(\tau) = \phi_0 + A\exp(-\tau/\tau_0)$, where ϕ_0, A, and τ_0 are fit parameters. The fit parameter values for this study were found to be $\phi_0 = 0.79$, $A = -1.39 \times 10^{-2}$, and $\tau_0 = 2.27$. As a result, Fig. 6 reveals that the packing fraction exponentially approaches a final steady-state packing fraction, in agreement with the previous results reported by Bandi et al.[15] Figure 6 shows the mean over nine experimental runs, with the error bars being their standard error.

3.2 *Force per disk*

The force on each disk in the granular pack was measured by the method described in Sects. 2.3.2 and 2.3.3. Figure 7 shows the cumulative number distribution of the force per disk at each tapping number τ in the granular pack. The range of the force per disk F_d in Fig. 7 is wider than the calibration range [Fig. 4(c)]. However, the calibration is performed under 1D diametral compression, i.e., the coordination number is 2 in the calibration. In the granular pack, on the other hand, the average coordination number is almost 4. Thus, the force applied to each disk can be approximately 2 times greater than that in the calibration. Thus, the force magnitude of each contact point in the granular pack is

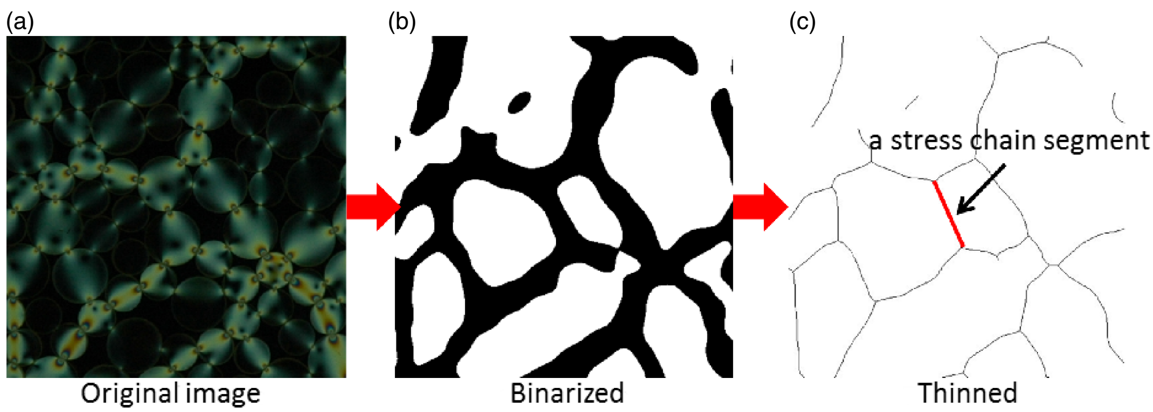

Fig. 5. (Color online) Method of stress chain thinning and definition of stress chain segment length. A thinned stress chain (c) is obtained by binarizing the original image [(a) → (b)] and thinning it [(b) → (c)]. A stress chain segment length is defined by the linear distance between intersections or end points in the thinned stress chain image.

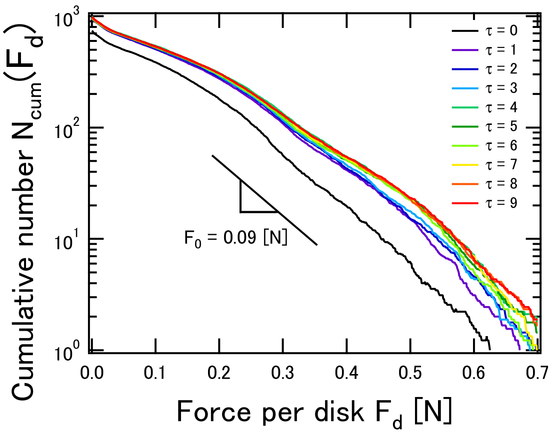

Fig. 7. (Color online) Cumulative number distributions of force per disk at each tapping number τ in a log-linear scale. The black solid line represents the initial configuration ($\tau = 0$) whereas the colored lines represent the compacted states for various τ values. The data represent the mean value of nine experimental runs.

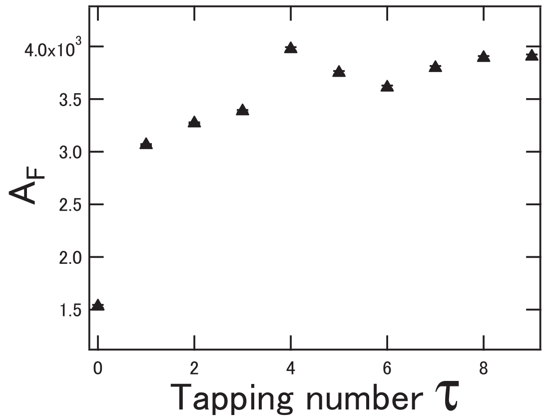

Fig. 8. Variation of fit parameter A_F as a function of tapping number τ. A_F increases with each manual tapping. The A_F values are calculated from the fitting using Eq. (1) with fixed F_0 (= 0.09 N). The error bars represent the uncertainty of the fitting.

almost within the calibration range. The distribution can be approximated by the exponential form:

$$N_{cum}(F_d) = A_F \exp\left(-\frac{F_d}{F_0}\right), \tag{1}$$

where $N_{cum}(F_d)$ is the number of disks on which the applied force is greater than or equal to F_d. A_F and F_0 are fit parameters with F_0 having the dimension of force. Figure 7 is obtained from the mean value of nine identical experimental runs, and exhibits a roughly exponential distribution with almost constant slopes across all values of τ for the initial as well as the final compact state. The fit parameters were found to be $A_F = 1.53 \times 10^3$ and $F_0 = 9.06 \times 10^{-2}$ N at the initial configuration ($\tau = 0$). This result suggests that the functional form of the cumulative force distribution itself is invariant to the compaction under manual tapping as it yields the same slope for the exponential tail for all τ values. This result is qualitatively consistent with the previous study in which Liu et al. and Coppersmith et al. measured the cumulative distribution of force exerted by a three-dimensional (3D) granular pack on the container walls and showed that it follows an exponential distribution.[21,22] Note that, however, the coefficient A_F does vary with τ, as shown in Fig. 8.

3.3 Force chain segment length

Recent studies have analyzed force chain segment lengths under pure shear and isotropic compression and found that they are exponentially distributed:[23–25]

$$N_{cum}(l) = A_l \exp\left(-\frac{l}{l_0}\right), \tag{2}$$

where $N_{cum}(l)$ is the number of segments of length greater than or equal to l. A_l and l_0 are fit parameters and l_0 has the dimension of length. The unit of length used is the mean disk diameter $D = (0.015 + 0.01)/2 = 0.0125$ m.

In agreement with previous works, the cumulative number distribution for the force chain segment length in this study is also found to be exponentially distributed (Fig. 9) with the functional form of Eq. (2). The fit parameters are $A_l = 9.45 \times 10^2$ and $l_0 = 0.82D \simeq 0.01$ m at the initial configuration ($\tau = 0$). The characteristic length l_0 corresponding to the diameter of the small disk is derived from a mere reflection of the effect on the analysis method. This fact indicates that a segment length is meaningless for less than the small disk size. This is natural because we consider the force chain structure to consist of disks. This is also clearly reflected in Fig. 9, where a steady exponential slope is observed only for $l > 1D$. The slope and coefficient of the exponential distributions are almost constant across all τ values, rendering this distribution invariant to the manual tapping protocol.

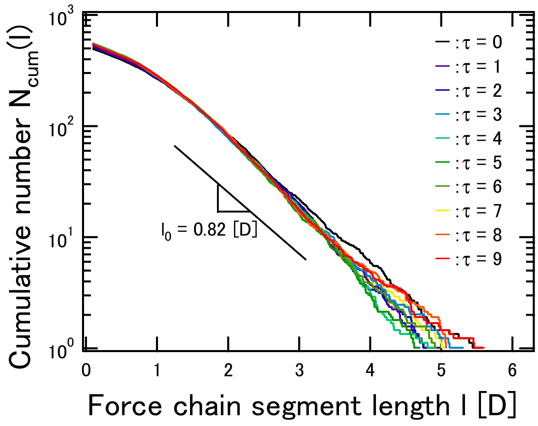

Fig. 9. (Color online) Cumulative number distributions of force chain segment lengths in a log-linear scale. The force chain segment lengths are quoted in the unit of the mean disk diameter D. The black solid line represents the initial configuration ($\tau = 0$) whereas the colored lines represent the compacted states for various τ values. The data represent the mean of nine experimental runs.

4. Discussion

The experimental results discussed thus far show that the packing fraction varies with the tapping number τ through the relationship $\phi(\tau) = \phi_0 + A\exp(-\tau/\tau_0)$ and that ϕ saturates at an asymptotic value of $\phi_0 = 0.79$. Additionally, the cumulative distribution of the force per disk at each τ was found to be exponentially distributed as $N_{cum}(F_d) = A_F \exp(-F_d/F_0)$. In particular, whereas the characteristic force F_0 remains invariant to τ, the coefficient A_F varies with

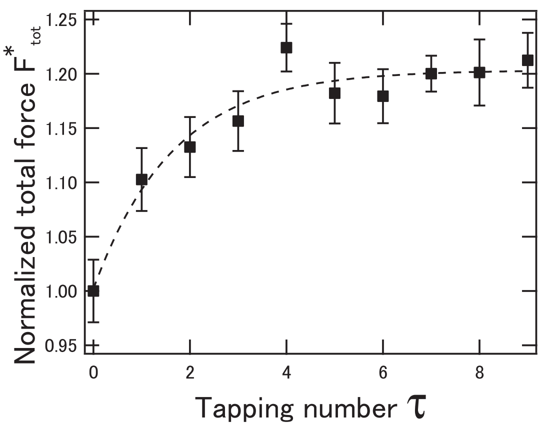

Fig. 10. Tapping number dependence of the normalized total force F^*_{tot}. The mean value of nine runs is shown, and the error bars represent the standard error of nine runs. The dashed curve is the fit, $F^*_{tot}(\tau) = F^*_{t0} + A^*_t \exp(-\tau/\tau_{t0})$, where $F^*_{t0} = 1.2$, $A^*_t = -0.2$, and $\tau_{t0} = 1.67$ are the values obtained for the fit parameters.

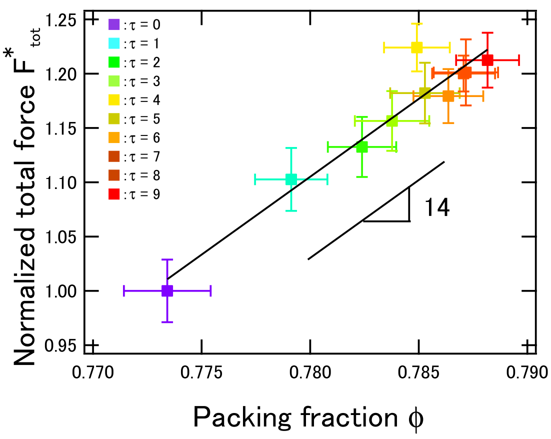

Fig. 11. (Color online) Relationship between F^*_{tot} and packing fraction ϕ. F^*_{tot} is defined by $F^*_{tot} \equiv F_{tot}(\tau)/F_{tot}(\tau = 0)$, where F_{tot} is the sum of the forces per disk in the granular pack. The mean value of nine runs is shown, and the error bars represent the standard error of nine runs. The black solid line indicates the linear relation, $[F^*_{tot}(\tau) - F^*_{t0}]/[\phi(\tau) - \phi_0] = 14 \pm 2$.

τ (Fig. 8). On the other hand, the cumulative distribution of the force chain segment length, which is also exponentially distributed $[N_{cum}(l) = A_l \exp(-l/l_0)]$, exhibits no dependence on the tapping number τ (Fig. 9). This suggests that the evolution of the packing fraction $\phi(\tau)$ leads to the increase in the internal force within the compacted granular pack, but does not lead to the creation of new force chain segments. On the basis of these trends, we now explore a speculative relationship between $\phi(\tau)$ and the total force F_{tot} of the granular pack. Since ϕ is a globally averaged structural quantity, it should be compared with the total force.

The total force F_{tot} is defined as $F_{tot} = \sum_{i=1}^{k} F_i$, where F_i is the force per disk on the ith disk, and the summation is carried over all disks in the granular pack (k represents the total number of disks), with the force threshold set at 0.1 N; forces below this threshold are not included in the summation. The total force is measured for the initial configuration and after each manual tap. Accordingly, we define the normalized total force as $F^*_{tot}(\tau) \equiv F_{tot}(\tau)/F_{tot}(\tau = 0)$, where $F_{tot}(\tau = 0)$ represents the total force of the initial configuration. In Fig. 10, we show the normalized total force F^*_{tot} as a function of τ. We can confirm the asymptotic behavior of $F^*_{tot}(\tau) = F^*_{t0} + A^*_t \exp(-\tau/\tau_{t0})$, where $F^*_{t0} = 1.2$, $A^*_t = -0.2$, and $\tau_{t0} = 1.67$. This functional form is similar to that for $\phi(\tau)$. The comparison of $\phi(\tau)$ and $F^*_{tot}(\tau)$ reveals that $\tau_{t0} \simeq \tau_0$. Therefore, the ratio $[F^*_{tot}(\tau) - F^*_{t0}]/[\phi(\tau) - \phi_0]$ should be approximated by $A^*_t/A = 14$. We independently confirm that $F^*_{tot}(\tau)$ vs $\phi(\tau)$ scales linearly as shown in Fig. 11. The slope of this scaling is 14 ± 2, in excellent agreement with the estimated result. This linear relationship suggests that the process of compaction by tapping leads to the increase in the granular internal force in a linear fashion. This linear dependence may result from the optimal amplitude perturbation ($\Gamma \simeq 3$–4) representing the linear response regime of the system. Stronger perturbations may not exhibit a similar dependence between $F^*_{tot}(\tau)$ and $\phi(\tau)$. This linear relation could be potentially useful for the estimation of the increase in the internal force within the compacted granular pack from packing fraction measurements for applications that involve compaction processes.

In this study, we developed a systematic method of analyzing a 2D granular pack comprised of photoelastic disks. Using the developed method, granular compaction by manual tapping was analyzed. Although an interesting structural evolution was revealed in this study, this is still the first step to approach granular compaction by tapping using photoelastic disks. The result should be compared with the case of controlled tapping using an electromagnetic shaker. Further studies concerning this comparison are in progress at present. The result will be published elsewhere.

5. Conclusions

In this study, the structural evolution of a 2D compacted granular pack has been experimentally studied using photoelastic disks. First, we developed a method of measuring the packing fraction, contact forces, and force chain segment lengths by image analysis methods. Then, the dependences of these quantities on manual tapping were experimentally measured. From the experimental results, the exponentially asymptotic behavior of the packing fraction was observed. The distributions of the applied force per disk and force chain segment length at each τ were found to be characterized by exponential forms. Although the former depends on the tapping number τ, the latter does not depend on it. The τ-dependent total force was also shown to exhibit the asymptotic exponential behavior. The linear relationship between these two functions (ϕ and F^*_{tot}) was confirmed from the measurements of F^*_{tot} and ϕ.

Acknowledgments

The authors acknowledge S. Watanabe, H. Kumagai, S. Sirono, and T. Morota for fruitful discussions and suggestions. H. Katsuragi was supported by JSPS KAKENHI Grant Number 26610113. M. M. Bandi was supported by the Collective Interactions Unit at the Okinawa Institute of Science and Technology Graduate University.

*katsurag@eps.nagoya-u.ac.jp

1) H. Katsuragi, *Physics of Soft Impact and Cratering* (Springer, Tokyo, 2015).

2) J. B. Knight, C. G. Fandrich, C. N. Lau, H. M. Jaeger, and S. R. Nagel, Phys. Rev. E **51**, 3957 (1995).
3) E. R. Nowak, J. B. Knight, M. L. Povinelli, H. M. Jaeger, and S. R. Nagel, Powder Technol. **94**, 79 (1997).
4) C. Josserand, A. V. Tkachenko, D. M. Mueth, and H. M. Jaeger, Phys. Rev. Lett. **85**, 3632 (2000).
5) J. A. Dijksman and M. van Hecke, Europhys. Lett. **88**, 44001 (2009).
6) P. Philippe and D. Bideau, Europhys. Lett. **60**, 677 (2002).
7) P. Philippe and D. Bideau, Phys. Rev. Lett. **91**, 104302 (2003).
8) G. Lumay and N. Vandewalle, Phys. Rev. Lett. **95**, 028002 (2005).
9) G. Lumay, F. Ludewig, and N. Vandewalle, J. Phys.: Conf. Ser. **40**, 133 (2006).
10) D. Arsenović, S. Vrhovac, Z. Jakšić, L. Budinski-Petković, and A. Belić, Phys. Rev. E **74**, 061302 (2006).
11) P. Ribière, P. Richard, P. Philippe, D. Bideau, and R. Delannay, Eur. Phys. J. E **22**, 249 (2007).
12) D. Howell, R. P. Behringer, and C. Veje, Phys. Rev. Lett. **82**, 5241 (1999).
13) J. Geng, D. Howell, E. Longhi, R. P. Behringer, G. Reydellet, L. Vanel, E. Clécfment, and S. Luding, Phys. Rev. Lett. **87**, 035506 (2001).
14) T. S. Majmudar and R. P. Behringer, Nature **435**, 1079 (2005).
15) M. M. Bandi, M. K. Rivera, F. Krzakala, and R. E. Ecke, Phys. Rev. E **87**, 042205 (2013).
16) J. G. Puckett and K. E. Daniels, Phys. Rev. Lett. **110**, 058001 (2013).
17) H. Zheng, J. A. Dijksman, and R. P. Behringer, EPL **107**, 34005 (2014).
18) R. P. Behringer, D. Bi, B. Chakraborty, A. Clark, J. Dijksman, J. Ren, and J. Zhang, J. Stat. Mech. **2014**, P06004 (2014).
19) M. D. Abràmoff, P. J. Magalhães, and S. J. Ram, Biophotonics Int. **11**, 36 (2004).
20) E. Clément, J. Duran, and J. Rajchenbach, Phys. Rev. Lett. **69**, 1189 (1992).
21) C.-h. Liu, S. R. Nagel, D. A. Schecter, S. N. Coppersmith, S. Majumdar, O. Narayan, and T. A. Witten, Science **269**, 513 (1995).
22) S. N. Coppersmith, C.-h. Liu, S. Majumdar, O. Narayan, and T. Witten, Phys. Rev. E **53**, 4673 (1996).
23) J. F. Peters, M. Muthuswamy, J. Wibowo, and A. Tordesillas, Phys. Rev. E **72**, 041307 (2005).
24) L. Sanfratello, J. Zhang, S. Cartee, and E. Fukushima, Granul. Matter **13**, 511 (2011).
25) L. Zhang, Y. Wang, and J. Zhang, Phys. Rev. E **89**, 012203 (2014).